Supporting Information

Hierarchical Glucose-intercalated NiMn-G-LDH@NiCo$_2$S$_4$ Core-Shell Structure as Binder-Free Electrode for Flexible All-Solid-State Asymmetric Supercapacitors

Shixia Chen[†,§], Chengxi Lu [‡], Lu Liu[†], Mai Xu [§], Jun Wang[†,*], Qiang Deng[†], Zheling Zeng[†], Shuguang Deng [§,*]

[†] Key Laboratory of Poyang Lake Environment and Resource Utilization, Ministry of Education, School of Resources Environmental & Chemical Engineering, Nanchang University, Nanchang, 330031, China

[‡] School for Molecular Sciences, Arizona State University, 550 E. Tyler Mall, Tempe, AZ 85287, USA

[§] School for Engineering of Matter, Transport and Energy, Arizona State University, 551 E. Tyler Mall, Tempe, AZ 85287, USA

*Corresponding author:

1. E-mail: shuguang.deng@asu.edu (S. Deng)

2. E-mail: jwang7@ncu.edu.cn (J. Wang)

Table of contents

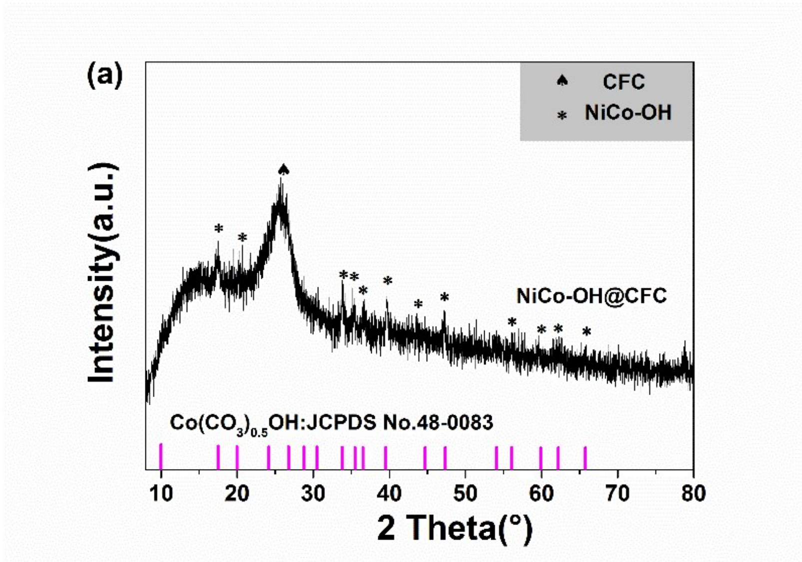

Fig. S1. XRD patterns of NiCo-OH@CFC

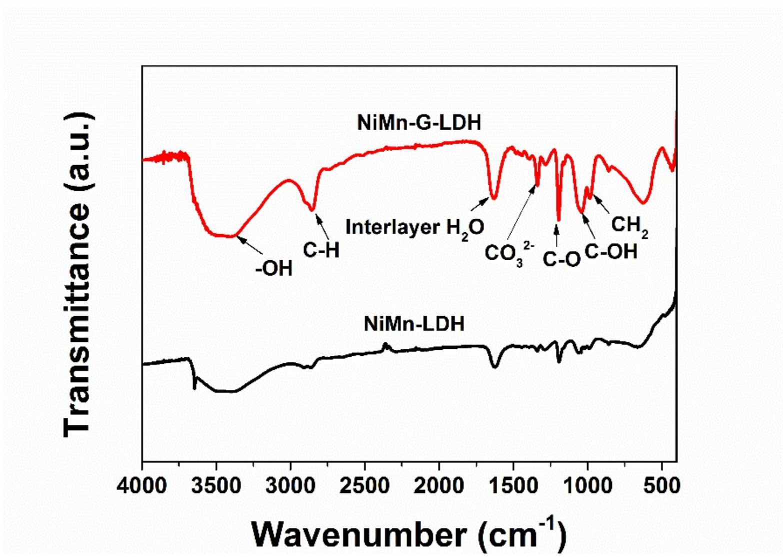

Fig. S2. FT-IR spectra of NiMn-LDH and NiMn-G-LDH

FT-IR was performed to further verify the glucose intercalation. As shown in Fig. S2, the strong and broad absorption in the range of 3400-3600 cm^{-1} and the peak at 1632 cm^{-1} was observed in both samples, which can be ascribed to -OH and interlayer H_2O of LDH. [1] The peaks in the range of 400-800 cm^{-1} are mainly assigned to the vibrations of Ni-O and Mn-O bonds in the LDHs. And the peaks centered at 1336 cm^{-1} and 1193 cm^{-1} are assigned to CO_3^{2-} and C-O, suggesting the CO_3^{2-} intercalation in both NiMn-LDH and NiMn-G-LDH, which is consistent with the XRD results. Specially, the double peaks around 2868

cm^{-1} and the obviously discerned peaks at 1042 and 985 cm^{-1} in the NiMn-G-LDH are due to stretching vibration of C-H, C-OH and CH_2, respectively, verifying the successful intercalation of glucose into the interlayer of NiMn-G-LDH. The result is consistent with the previous literatures. [2,3]

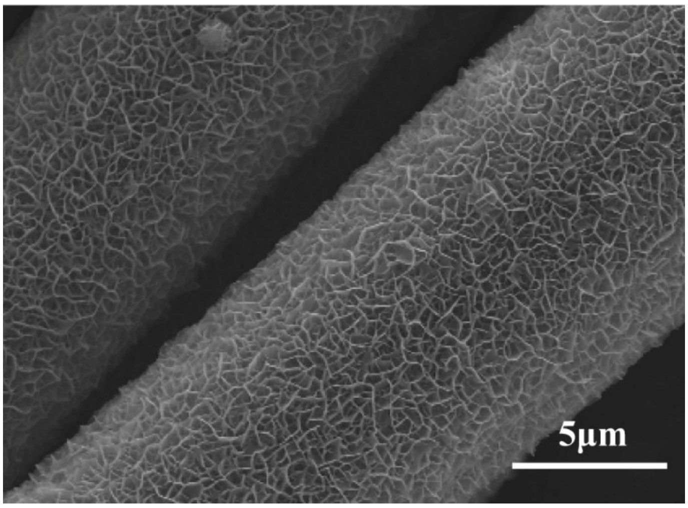

Fig. S3. SEM images of NiMn-G-LDH@CFC.

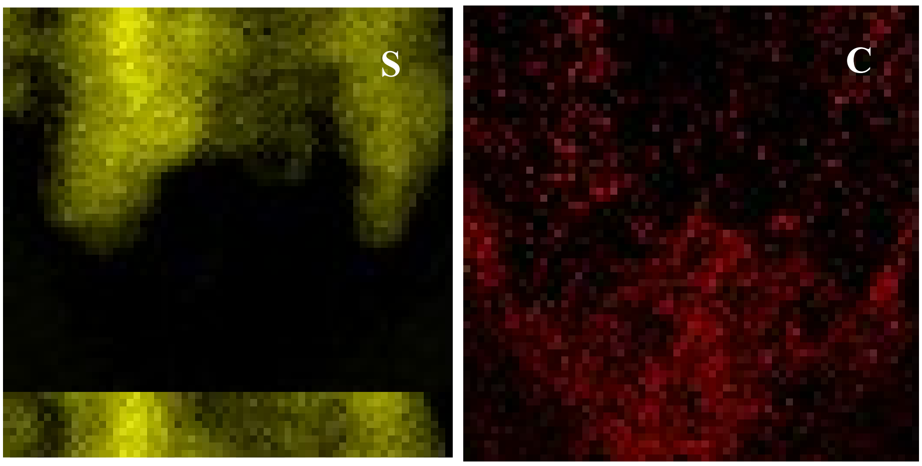

Fig. S4. EDS mapping images of S and C on NiMn-G-LDH@$NiCo_2S_4$ that were scratched from the CFC.

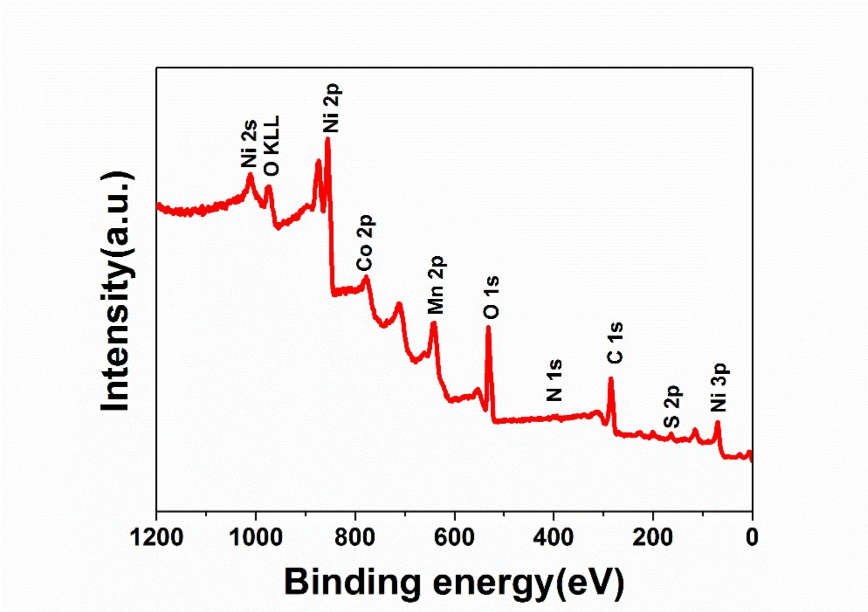

Fig. S5. XPS survey spectra of NiMn-G-LDH@$NiCo_2S_4$@CFC.

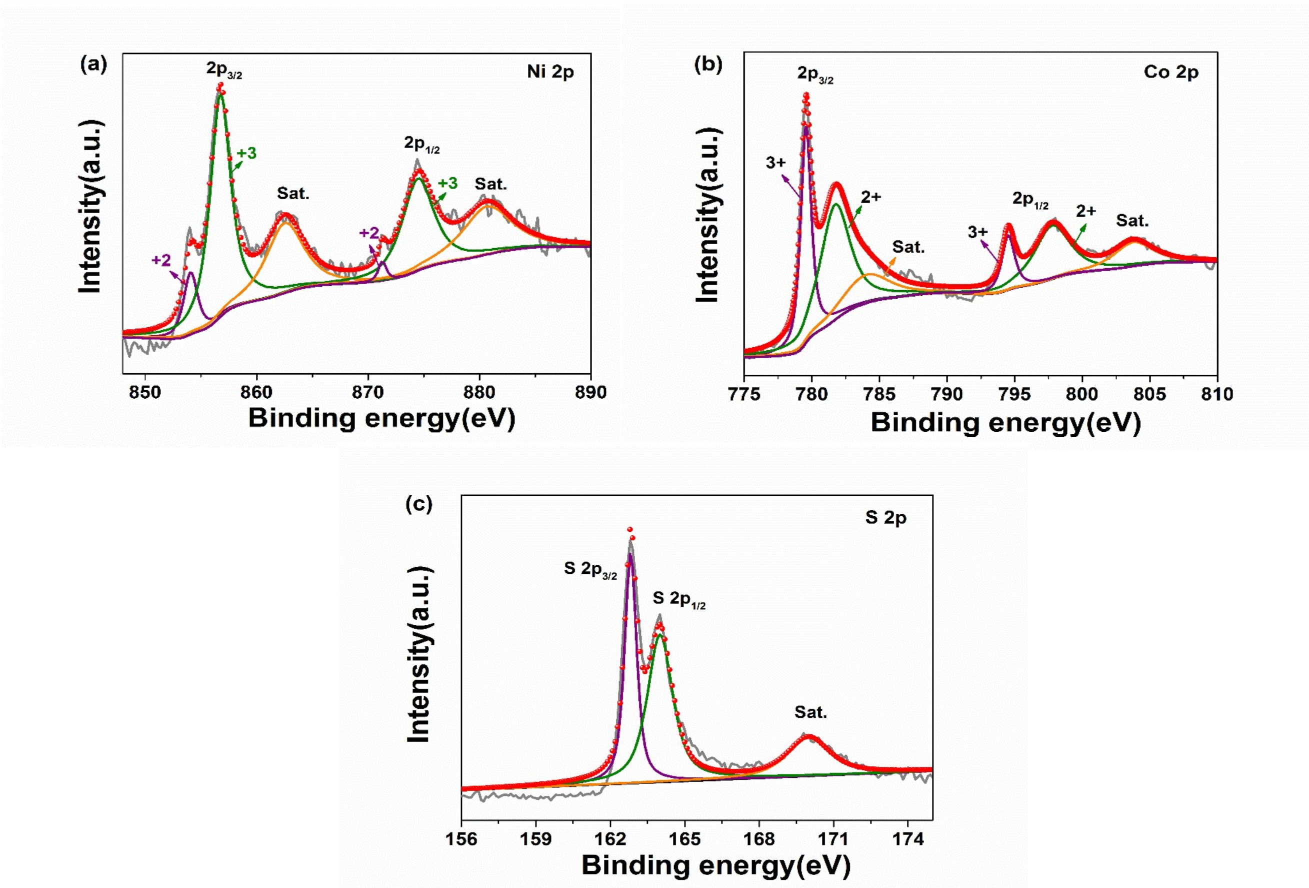

Fig. S6. (a)Ni 2p (b) Co 2p and (c) S 2p spectrum of $NiCo_2S_4$@CFC and (d) Mn 2p of NiMn-G-LDH@$NiCo_2S_4$@CFC.

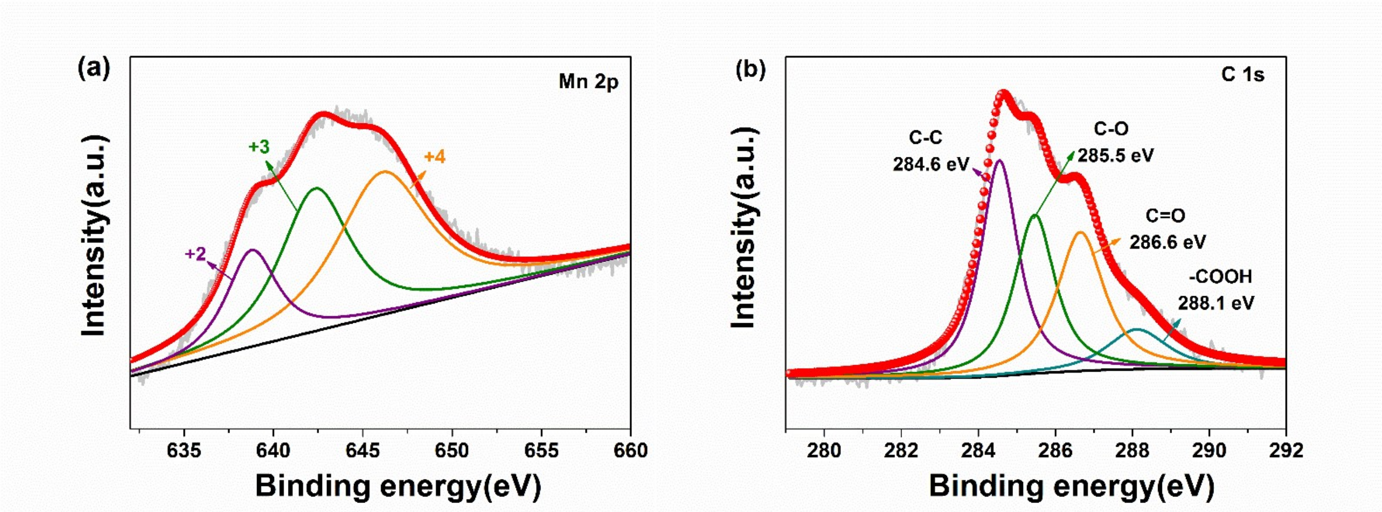

Fig. S7. (a)Mn 2p and (b) C 1s spectrum of of NiMn-G-LDH@$NiCo_2S_4$@CFC.

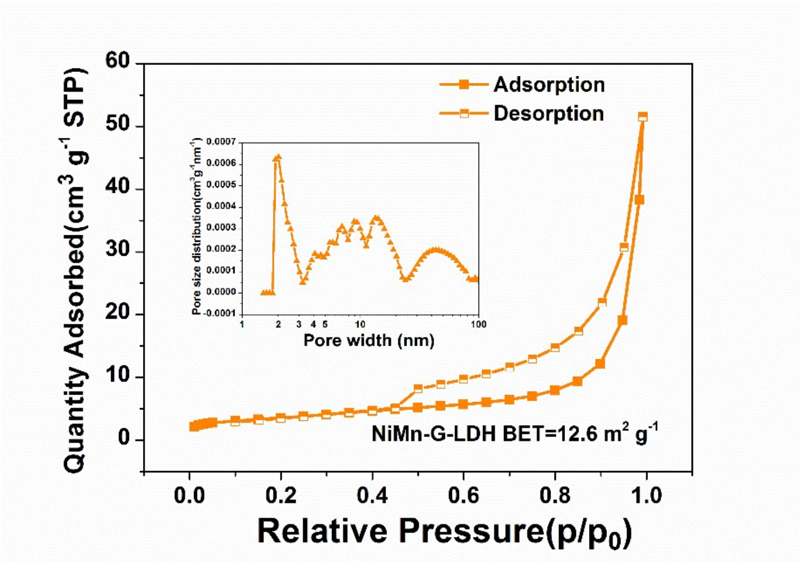

Fig. S8. N_2 adsorption-desorption isotherm and pore size distribution of the NiMn-G-LDH that were scratched from the CFC.

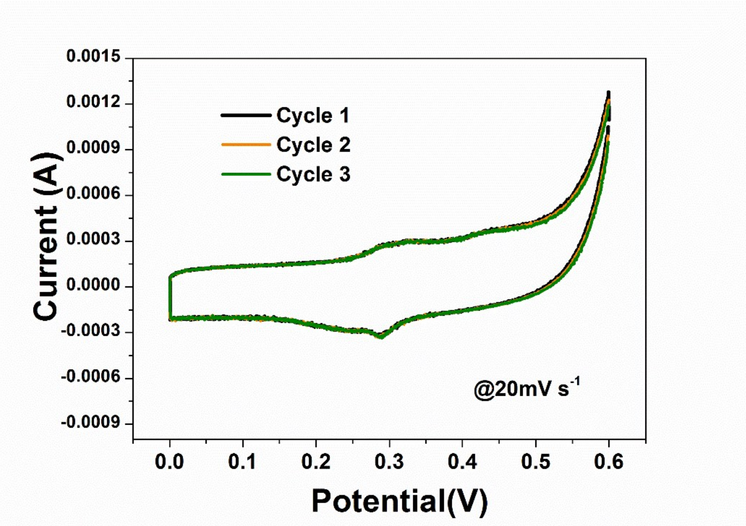

Fig. S9. CV curves of the pristine CFC at 20 mV s^{-1}.

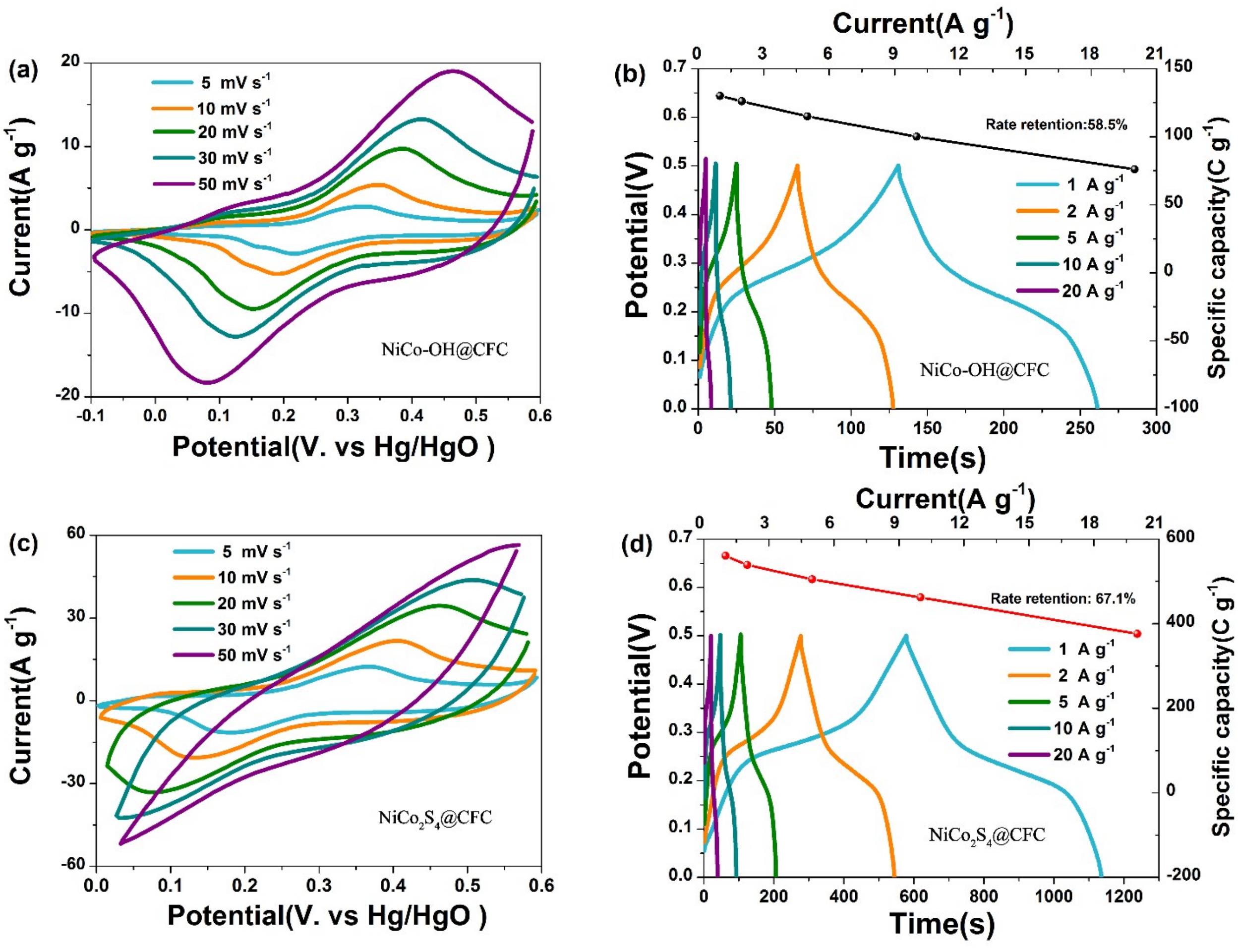

Fig. S10. (a) CV curves, (b) GCD curves and specific capacity at various current densities of NiCo-OH@CFC and (c) CV curves, (d) GCD curves and specific capacity at various current densities of $NiCo_2S_4$@CFC.

The electrochemical performance of NiCo-OH@CFC and $NiCo_2S_4$@CFC were investigated in a three-electrode configuration. Fig. S10a and S10c show the CV curves of the NiCo-OH@CFC and $NiCo_2S_4$@CFC electrodes at different scan rates ranging from 5 to 50 mV s^{-1}, respectively. Obviously, two pairs of similar well-defined redox peaks can be observed and the integrated CV area of $NiCo_2S_4$@CFC is much larger than that of the NiCo-OH@CFC, suggesting the improved specific capacitance by the sulfurization. Moreover, the calculated specific capacity based on the GCD of NiCo-OH@CFC and $NiCo_2S_4$@CFC are 130 C g^{-1} and 561 C g^{-1} at 1 A g^{-1}, respectively. With the increase of current density, the specific capacitance retention of 58.5% for the NiCo-OH@CFC electrodes is lower than that of 67.1 % for the $NiCo_2S_4$@CFC. The enhanced specific capacitance and rate retention can be attributed to the better electronic conductivity and faster redox reactions of $NiCo_2S_4$@CFC.

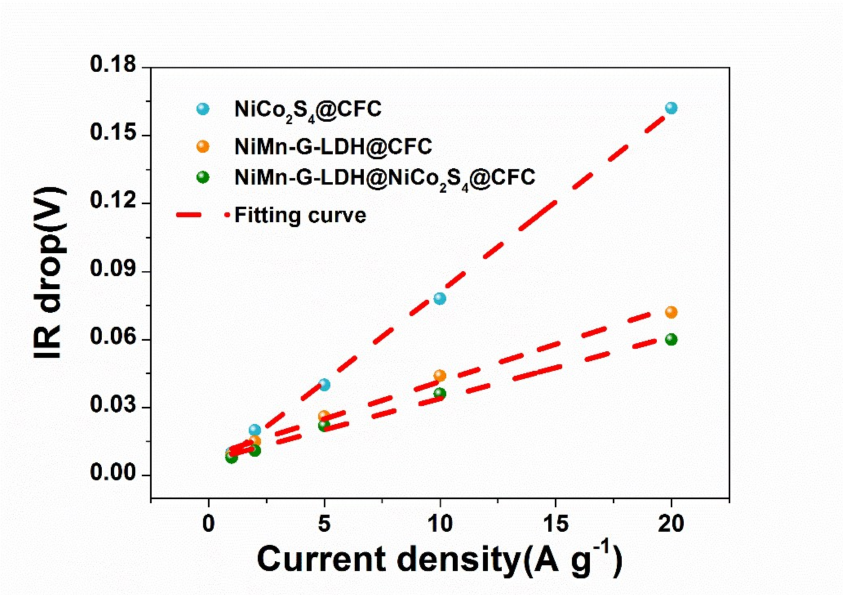

Fig. S11. IR drop of **NiMn-G-LDH**@CFC**, $NiCo_2S_4$**@CFC, **and NiMn-G-LDH@$NiCo_2S_4$**@CFC under various current densities.

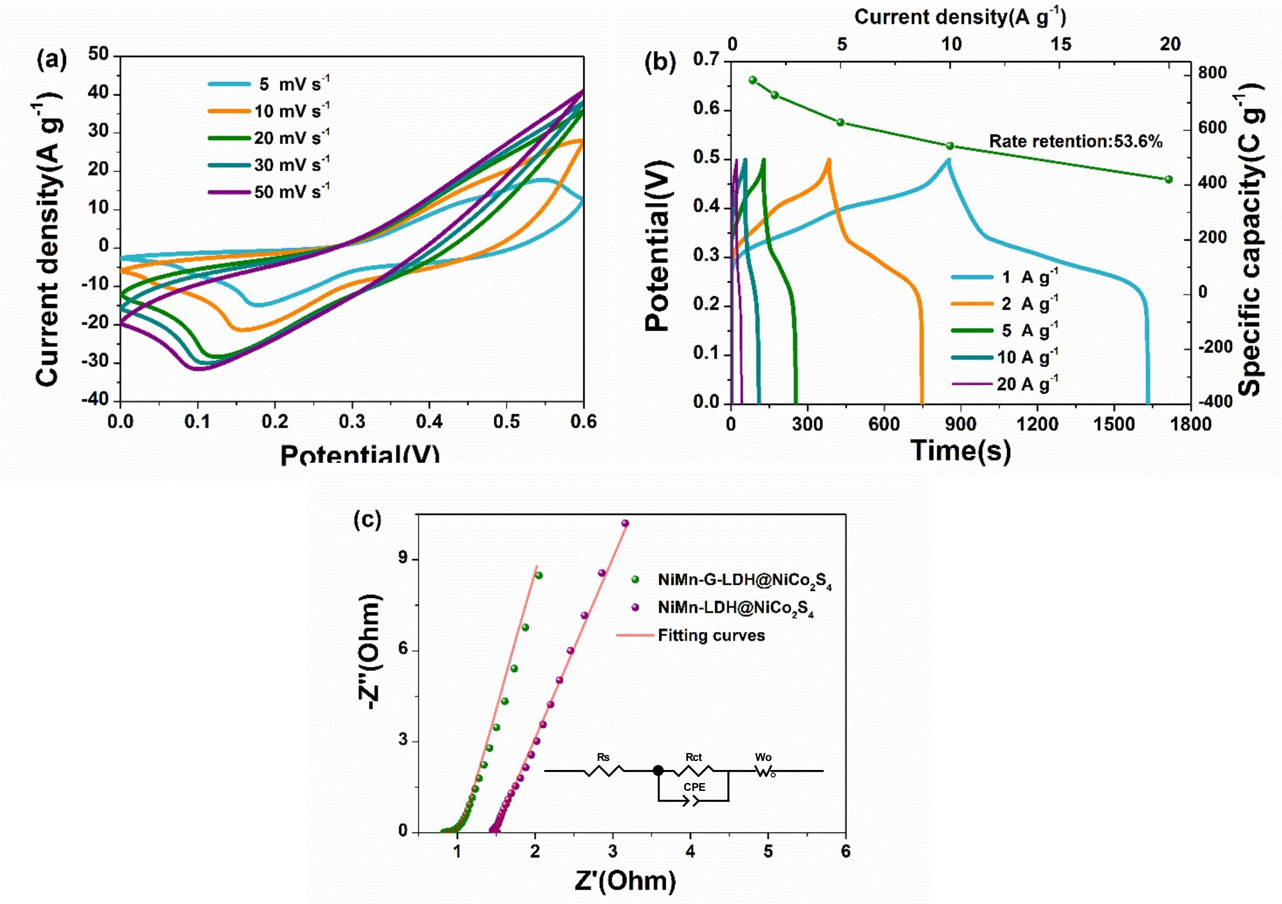

Fig. S12. (a) CV curves, (b) GCD curves and specific capacity at various current densities of NiMn-LDH @$NiCo_2S_4$@CFC and (c) EIS of NiMn-LDH@$NiCo_2S_4$@CFC and NiMn-G-LDH@$NiCo_2S_4$@CFC.

The corresponding electrochemical tests of NiMn-LDH@$NiCo_2S_4$@CFC were conducted as a control. As displayed in Fig. S12a, the CV curves deformed when the scan rate increased to above 30 mV s^{-1}, suggesting an inferior specific capacity retention. The calculated specific capacity based on the GCD of NiMn-LDH@$NiCo_2S_4$@CFC is 783 C g^{-1} at 1A g^{-1}, which is lower than that of NiMn-G-LDH@CFC (1018 C g^{-1}). Additionally, NiMn-LDH@$NiCo_2S_4$@CFC also exhibit lower specific capacitances retention of 53.6% than that of NiMn-G-LDH@$NiCo_2S_4$@CFC (68.4%) at 20 A g^{-1} (Fig. S12b). In order to better understand the improved ionic diffusion and charge transfer after glucose intercalation, the Nyquist plots of NiMn-LDH@$NiCo_2S_4$@CFC and NiMn-G-LDH@$NiCo_2S_4$@CFC were compared and fitted with the equivalent circuit model (Figure S12c). Upon glucose intercalation, NiMn-G-LDH@$NiCo_2S_4$@CFC possess smaller charge transfer resistance (R_{ct}, 0.37 Ω) and higher Warburg slope (W_o, 0.467) than those of NiMn-LDH@NiCo$_2$S$_4$@CFC (R_{ct}, 0.88 Ω and W_o, 0.452).[4,5]

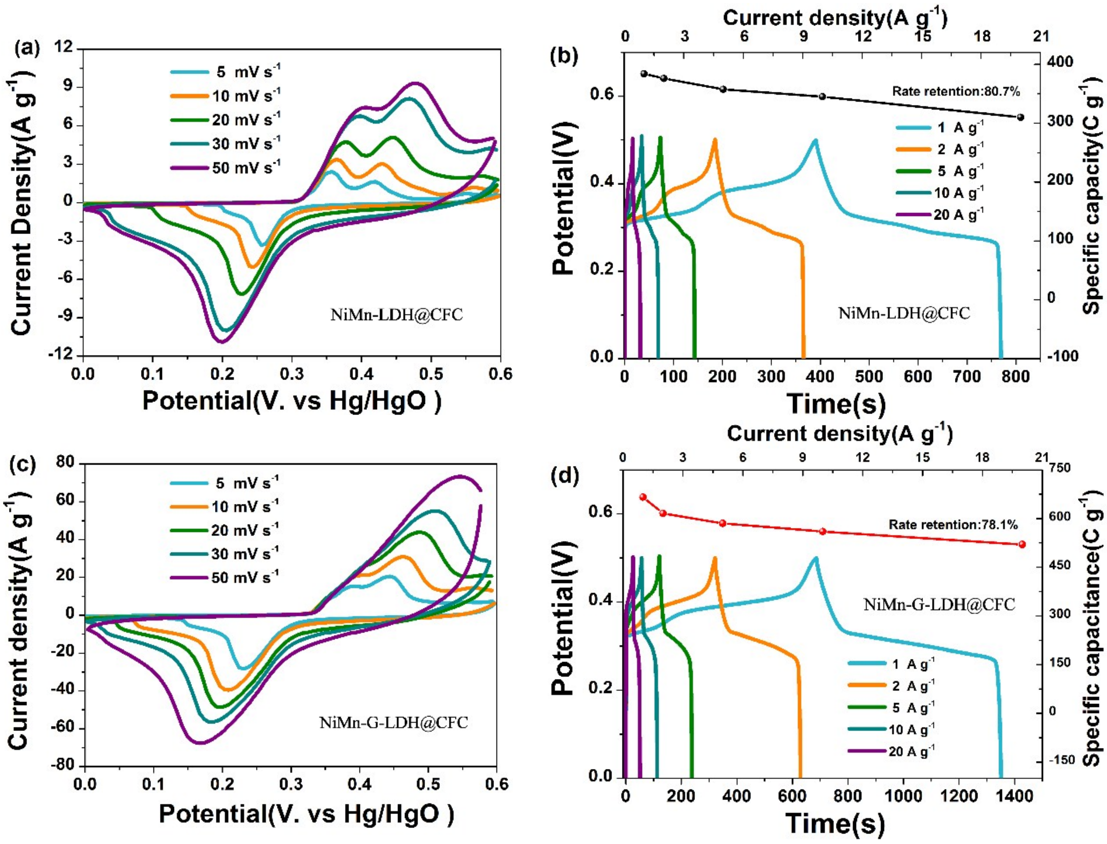

Fig. S13. (a) CV curves, (b) GCD curves and specific capacity at various current densities of NiMn-LDH@CFC and (c) CV curves, (d) GCD curves and specific capacity at various current densities of NiMn-G-LDH@CFC.

The electrochemical performance of NiMn-LDH@CFC and NiMn-G-LDH@CFC were also measured in a three-electrode system. The CV curves of the NiMn-LDH@CFC and NiMn-G-LDH@CFC electrodes also exhibit two pairs of similar well-defined redox peaks and the integrated CV area of NiMn-G-LDH@CFC is much larger than that of the NiCo-OH@CFC, implying the improved specific capacitance by the glucose intercalation (shown in Fig. S13a and S13c). Thus, the calculated specific capacity based on the GCD of NiMn-G-LDH@CFC is 666 C g^{-1}, which is much higher than that of 384 C g^{-1} for the NiMn-LDH@CFC at 1 A g^{-1}. Moreover, NiMn-G-LDH@CFC yield similar specific capacitance retention of 78.1%, compared with that of 80.1% for NiMn-LDH @CFC at 20 A g^{-1} even at a much higher initial capacitance.

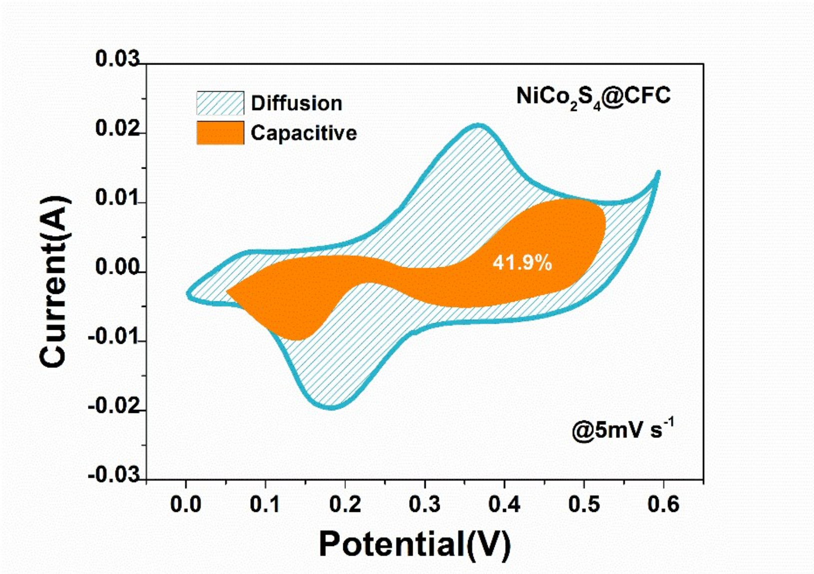

Fig. S14. Capacitive and diffusion-controlled contribution to the charge storage of $NiCo_2S_4$@CFC.

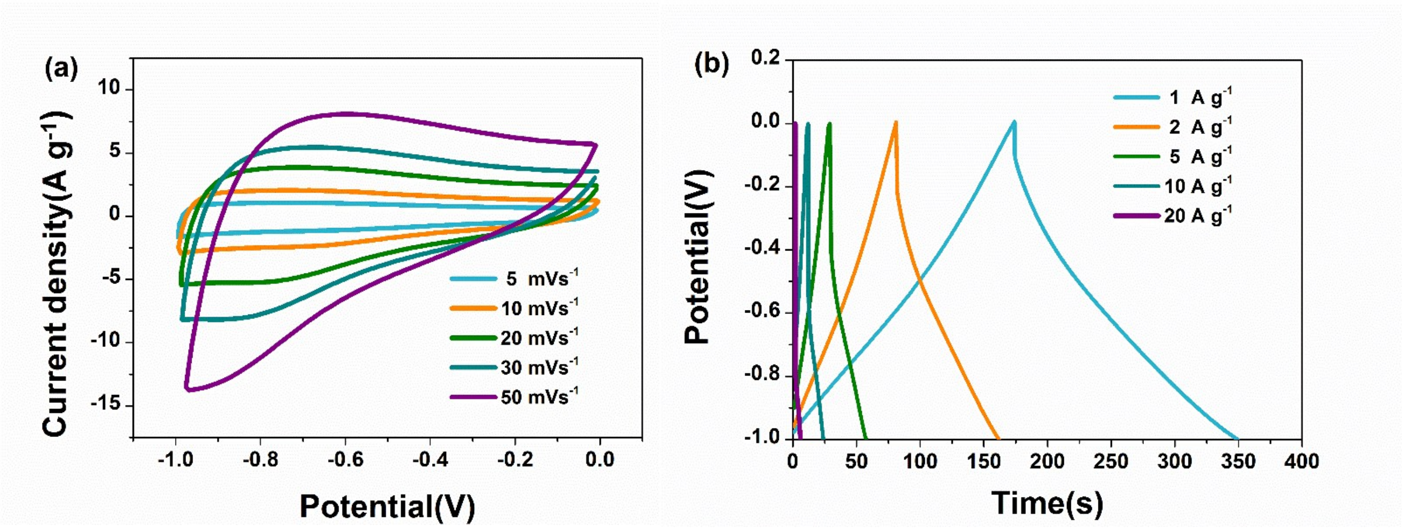

Fig. S15. (a) CV of AC negative electrode at different scanning rates and (b) GCD curves at different current densities

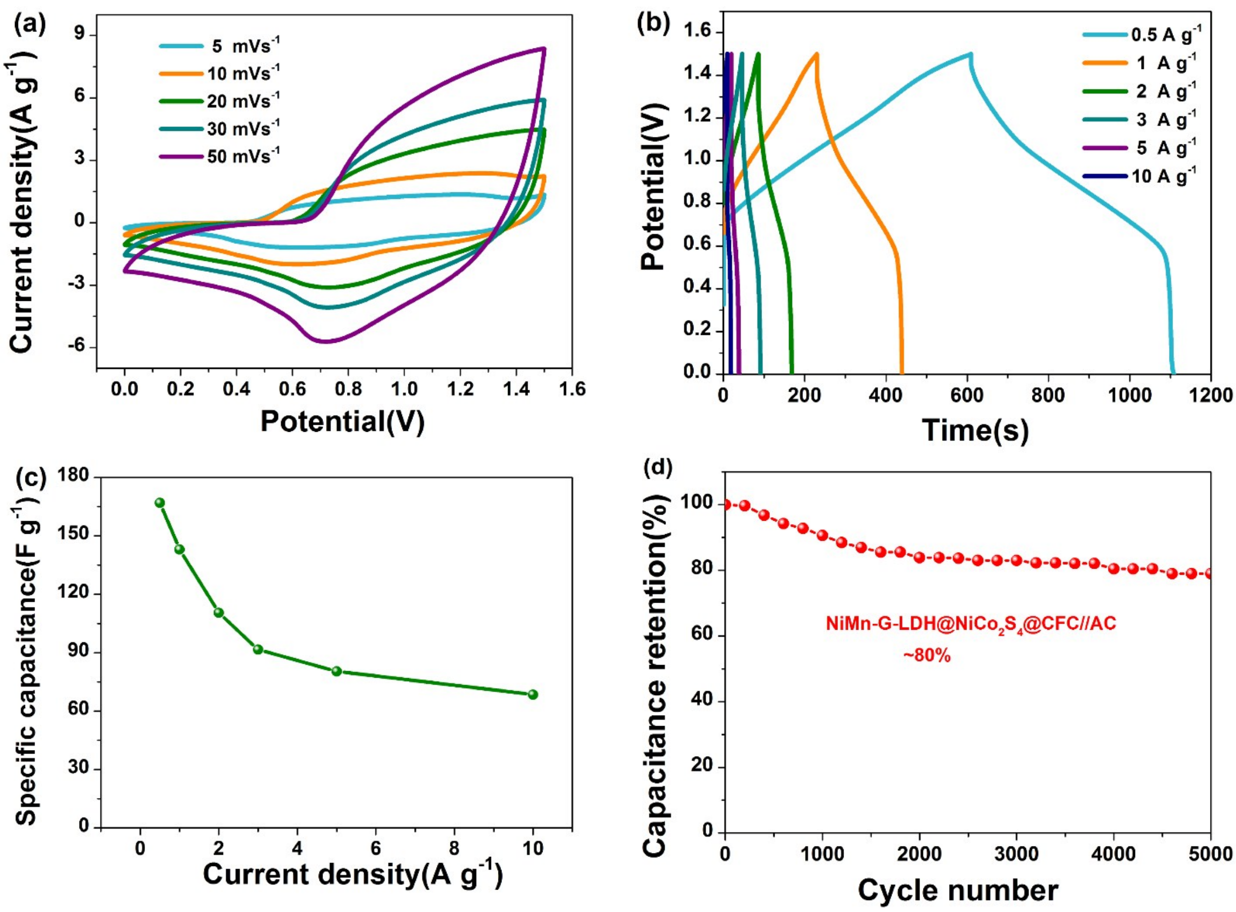

Fig. S16. Electrochemical performance of NiMn-G-LDH@$NiCo_2S_4$@CFC//AC assembled in aqueous system (a) CV and (b) GCD curves; (c) specific capacitances of the SASC device at various current densities; (d) cycling stability at a current density of 10 A g^{-1}.

Fig. S17. LED lighting test with two device connected in series

Table S1. Comparison of intercalated and un-intercalated LDH electrodes in the three-electrode system.

Electrode materials	Specific capacity (1 A g^{-1})	Specific capacity (20 A g^{-1})
NiMn-LDH@CFC	384 C g^{-1}	308 C g^{-1}
NiMn-G-LDH@CFC	666 C g^{-1}	520 C g^{-1}
NiMn-LDH@$NiCo_2S_4$@CFC	783 C g^{-1}	420 C g^{-1}
NiMn-G-LDH@$NiCo_2S_4$@CFC	1018 C g^{-1}	696 C g^{-1}

Table S2. Comparison of electrochemical performance of LDHs-based electrodes in the three-electrode system.

Electrode materials	Electrolyte	Specific capacitance	Rate capability	Ref.
NiMn-G-LDH@$NiCo_2S_4$@CFC	6M KOH	2036 F g^{-1} (1 A g^{-1})	68.4% at 20A g^{-1}	This work
NiMn-LDH/rGO	2 M KOH	1635 F g^{-1} (1 A g^{-1})	71.0% at 10 A g^{-1}	6
Glucose-intercalated NiMn-LDH	6 M KOH	1464 F g^{-1} (0.5 A g^{-1})	59.4% at 10 A g^{-1}	2
(Ni,Co)Se_2/NiCo−LDH@CFC	3 M KOH	1224 F g^{-1} (2 A g^{-1})	71.0% at 20 A g^{-1}	7
KCu_7S_4@NiMn LDH	1M LiOH	734 F g^{-1} (1 A g^{-1})	76.9% at 30 A g^{-1}	1
$NiCo_2O_4$@CNT	2 M KOH	1596 F g^{-1} (1 A g^{-1})	88.1% at 10 A g^{-1}	8

Table S3. The energy density and power density of various electrodes in an ASC system in references.

Asymmetric supercapacitor	Energy density	Power density	Ref.
NiMn-G-LDH@$NiCo_2S_4$@CFC // AC	60.3 Wh kg^{-1}	375 W kg^{-1}	This work
Core-shell NiCo-LDH/NiCoP@NiMn-LDH	42.2 Wh kg^{-1}	750 W kg^{-1}	9
Core-shell $NiCo_2S_4$@$Ni(OH)_2$@PPy	34.7 Wh kg^{-1}	120 W kg^{-1}	10
$NiCo_2S_4$ nanopetals //AC	35.6 Wh kg^{-1}	820 W kg^{-1}	11
Core-shell (Ni,Co)Se_2 /NiCo−LDH //AC	39.0 Wh kg^{-1}	1650 W kg^{-1}	7
Core-shell CoS_x/Ni-Co LDH//AC	35.8 Wh kg^{-1}	800 W kg^{-1}	12

References:

1 X. L. Guo, J. M. Zhang, W. N. Xu, C. G. Hu, L. Sun and Y. X. Zhang, *J. Mater. Chem. A*, 2017, **5**, 20579-20587.

2 L. Lv, K. Xu, C. Wang, H. Wan, Y. Ruan, J. Liu, R. Zou, L. Miao, K. (Ken) Ostrikov, Y. Lan and J. Jiang, *Electrochim. Acta*, 2016, **216**, 35-43.

3 M. Padmini, S. K. Kiran, N. Lakshminarasimhan, M. Sathish and P. Elumalai, *Electrochim. Acta*, 2017, **236**, 359-370.

4 M. Xu, Y. Liu, N. Fu, W. Lu, G. Zhang, H. Huang and L. Zhou, *Adv. Funct. Mater.*, 2017, **27**, 1605307.

5 M. Wang, Z. Li, C. Wang, R. Zhao, C. Li, D. Guo, L. Zhang and L. Yin, *Adv. Funct. Mater.*, 2017, **27**, 1701014.

6 M. Li, J. P. Cheng, J. Wang, F. Liu and X. B. Zhang, *Electrochim. Acta*, 2016, **206**, 108-115.

7 X. Li, H. Wu, C. Guan, Y. Dong, J. Wang, H. Wu, S. J. Pennycook, X. Li and A. M. Elshahawy, *Small*, 2018, **15**, 1803895.

8 P. Wu, S. Cheng, M. Yao, L. Yang, Y. Zhu, P. Liu, O. Xing, J. Zhou, M. Wang, H. Luo and M. Liu, *Adv. Funct. Mater.*, 2017, **27**, 1702160.

9 H. Liang, J. Lin, H. Jia, S. Chen, J. Qi, J. Cao, T. Lin, W. Fei and J. Feng, *J. Mater. Chem. A*, 2018, **6**, 15040-15046.

10 M. Liang, M. Zhao, H. Wang, J. Shen and X. Song, *J. Mater. Chem. A*, 2018, **6**, 2482-2493.

11 Y. Wen, S. Peng, Z. Wang, J. Hao, T. Qin, S. Lu, J. Zhang, D. He, X. Fan and G. Cao, *J. Mater. Chem. A*, 2017, **5**, 7144-7152.

12 X. Guan, M. Huang, L. Yang, G. Wang and X. Guan, *Chem. Eng. J.*, 2019, **372**, 151-162.